Materials Science and Engineering C 29 (2009) 2398–2410

Contents lists available at ScienceDirect

Materials Science and Engineering C

journal homepage: www.elsevier.com/locate/msec

The role of organic intertile layer in abalone nacre

M.A. Meyers [a,*], C.T. Lim [b], A. Li [b], B.R. Hairul Nizam [b], E.P.S. Tan [b], Y. Seki [a], J. McKittrick [a]

[a] University of California, San Diego, La Jolla, California, USA
[b] National University of Singapore, Singapore, Republic of Singapore

ARTICLE INFO

Article history:
Received 17 June 2009
Accepted 3 July 2009
Available online 13 July 2009

Keywords:
Chitin
Abalone
Nacre

ABSTRACT

Characterization of the growth surfaces removed from red and green abalone (*Haliotis*) shells shows a terraced cone mode of mineralization in which the organic layer is deposited periodically and regulates the formation of tiles with ~500 nm thickness. The details of the mineral and organic layer surface are revealed by atomic force microscopy; the surface roughness and the thickness of the tiles in the terraces and organic intertile layer were measurement. Nanoindentation experiments at the top of the terraced cones confirm a hardness of the same order as that of completely mineralized surfaces. Indentation of the organic layer provides a force-deflection curve that can be expressed as tension on a centrally-loaded membrane. The results show that the dry organic layer is very stiff and deforms inelastically or cracks under the indenter, whereas in the fully hydrated state it shows a low modulus and strength and great extensibility. This strongly suggests that this organic interlayer acquires considerable strength and stiffness as a result of the drying process, which is consistent with a T_g of approximately 200 °C for chitin. The chitin network that forms the structural component of the intertile layer is revealed and the orientation and spacing are measured. Terraced cones broken under the force of a flexing and shrinking organic layer enable the estimation of the tensile strength of the abalone when loaded through the fracture of the mineral bridges. Calculations show consistency with earlier tensile strength measurements of <10 MPa.

1. Introduction

The process by which shells are formed constitutes one of the most fascinating and complex topics of biomineralization (e.g., Mann [1]). With rare exceptions (such as in the case of the *Lingula* shell) calcium carbonate is the mineral component of shells, in both the calcitic and aragonitic forms. The microstructures observed vary greatly (e.g., Kobayashi and Samata [2]) and have been classified into prismatic, nacreous, foliated, and cross-lamellar. Four typical structures are shown in Fig. 1. A fibrous structure consisting of long rods has been observed in a *Patella* shell from Jeju Island, South Korea (Fig. 1a). The cross-lamellar structure characteristic of the conch shell (*Strombus gigas*, also found in bivalves, such as *Saxidomus purpuratus* is shown in Fig. 1b. The giant conch (*Tridacna gigas*) has been found to contain, in the inside, long aragonite crystals that can grow rapidly (Fig. 1c). However, by far the most studied microstructure is the nacreous platelet arrangement characteristic of the abalone shell (*Haliotis*, Fig. 1d). This article will focus on this shell, and primarily on the role that the organic intertile layer plays in the structure and growth.

The growth of nacre (structure seen in Fig. 1d) was first characterized by scanning electron microscopy by Bevelander and Nakahara [3,4]), Wada [5], Nakahara et al. [6–9], and Mutvei [10]. Additional contributions of note are the work by Fritz et al. [11,12]; Belcher et al. [13–15]; Shen et al. [16]; Schäffer et al. [17]; Zaremba et al. [18]; Sarikaya et al. [19–22]; and Nakahara [9]. There are significant differences among the different mollusks, but it is generally accepted that in most of the gastropods shells the "terraced cone" growth mode is prevalent, whereas bivalves are characterized by the "growth terraces" mode. More recently, Cartwright and Checa [23], Lin et al. [23–26] and Meyers et al. [27] investigated the detailed mechanisms of the 'terraced cone' growth through which the inter-digitated morphology of parallel tiles is formed. The identification of bridges between adjacent layers originating from subsurface tiles and extending through the organic matrix carried out by Song et al. [28,29] confirms the presence of mineral bridges; a growth model was first proposed by Schäffer et al. [17]. Indeed, Sarikaya et al. [19] identified the crystallographic orientations of different tiles on a stack and found them to be identical.

The objective of the research whose results are presented herein is to use novel characterization methods, viz., scanning electron microscopy, atomic force microscopy and nanoindentation, to further our understanding of the growth process.

2. Experimental techniques

For the purposes of this investigation, *Haliotis* shells from two sources were used:

Scripps Institution of Oceanography. Tanks with direct access to continuously circulating sea water and providing fresh sea water provided

* Corresponding author. Tel.: +1 858 534 4719; fax: +1 858 534 5698.
E-mail address: mameyers@ucsd.edu (M.A. Meyers).

0928-4931/$ – see front matter © 2009 Elsevier B.V. All rights reserved.
doi:10.1016/j.msec.2009.07.005

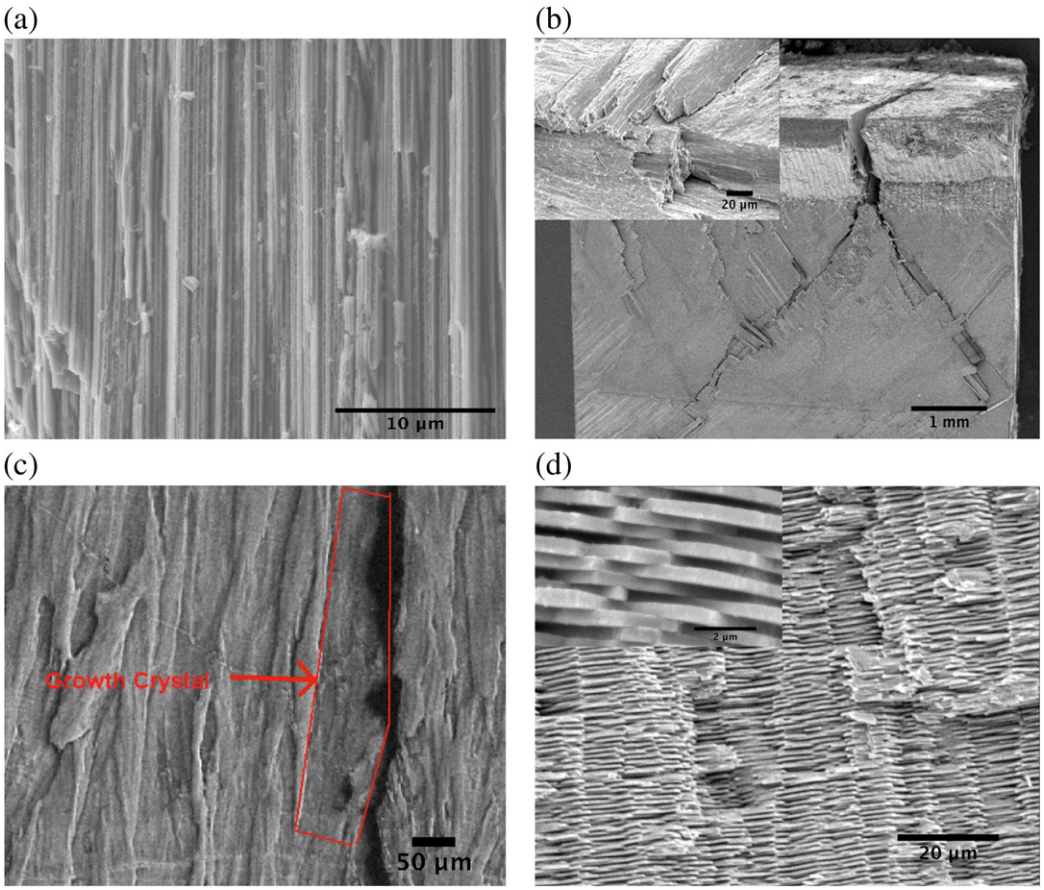

Fig. 1. Different structural morphologies encountered in shells; (a) fibrous structure, Jeju Island *Patella* shell; (b) cross lamellar structure, *Strombus* conch; (c) prismatic growth, *Tridacnas,* giant conch; (d) nacreous structure, *Haliotis*, abalone.

a natural environment with steady pH and realistic temperature fluctuations around a mean temperature of approximately 16°C. All animals were fed giant kelp (*Macrocystis pyrifera*) on a regular schedule. These shells were preserved in sea water after extraction of the animal and transported to Singapore. Approximately three specimens were characterized within 10 days of extraction from the tanks. These shells are from red abalone (*Haliotis rufescens*) that were described in earlier work by Lin et al. [24,25] and Meyers et al. [27]. They were characteristically 90 mm in maximum diameter. A typical shell being prepared for the extraction of specimens is shown in Fig. 2a.

Jeju Island, Korea. These are specimens of green abalone (*Haliotis fulgens*), which grow faster than red abalone but have a thinner shell. These shells were characteristically 40–60 mm in maximum diameter.

There are minor differences between the red (*rufescens*) and green (*fulgens*) abalone (*Haliotis*) shells. The green abalone tends to have a smaller thickness and 5–7 open respiratory holes; the red abalone has 3 or 4 open holes. Characteristically, the red abalone lives at greater depth.

Three methods (shown in Fig. 2b) were used to extract specimens from the growth surfaces of abalone. The growth surface is the one opposite to the exterior surface. Schäffer et al. [17], Zaremba et al. [18], and Lin et al. [24,26] used the flat pearl technique to extract specimens for growth observations; this consists of withdrawing the mantle with the epithelial layer, gluing a glass slide to the nacreous growth surface, and removing it after periods of 1–6 weeks. The second method, introduced by Lin et al. [26] consists of trepanning the shell with a coring drill, removing the core, and reinserting it. This core can then be re-extracted easily for observation after prescribed periods. The third method, which proved to be the easiest, is to simply saw off triangular sections of the growth region and directly observe them.

Scanning electron microscopy was conducted both in the environmental mode with specimens that had been dried for 2 h after being removed from wet shell and in the high vacuum mode, on specimens that had been carbon coated for increased resolution. Atomic force microscopy (Digital Instruments) was used to image the surface morphology of the specimens in contact mode. The latter experiments were conducted both in the wet and dry modes. Nanoindentation was carried out using a Berkovich tip on a Hysitron nanoindentation system.

3. Results and discussion

3.1. Characterization of growth surfaces

The discussion in this section is based on SEM observations. Fig. 3 shows the top view of the growth surface in the red abalone viewed in the environmental mode. Two features are evident: lighter round regions spaced approximately 5–10 μm apart, and a darker background. The light regions are the tops of the 'terraced growth' cones and the darker region is the organic layer. In some places, there are lighter streaks between the round features (marked with arrows). These segments have been previously been identified by Lin et al. [26] as tent-like folds in the organic layer. Fig. 3(c and d) show cracks in the organic layer which reveal the terraced cone growth underneath. There is growth of 2–3 layers above the organic layer, indicated by arrows 1, 2, 3 in Fig. 3d. This is evidence that the organic layer sags between growth cones. Meyers et al. [27] used this sag to estimate the

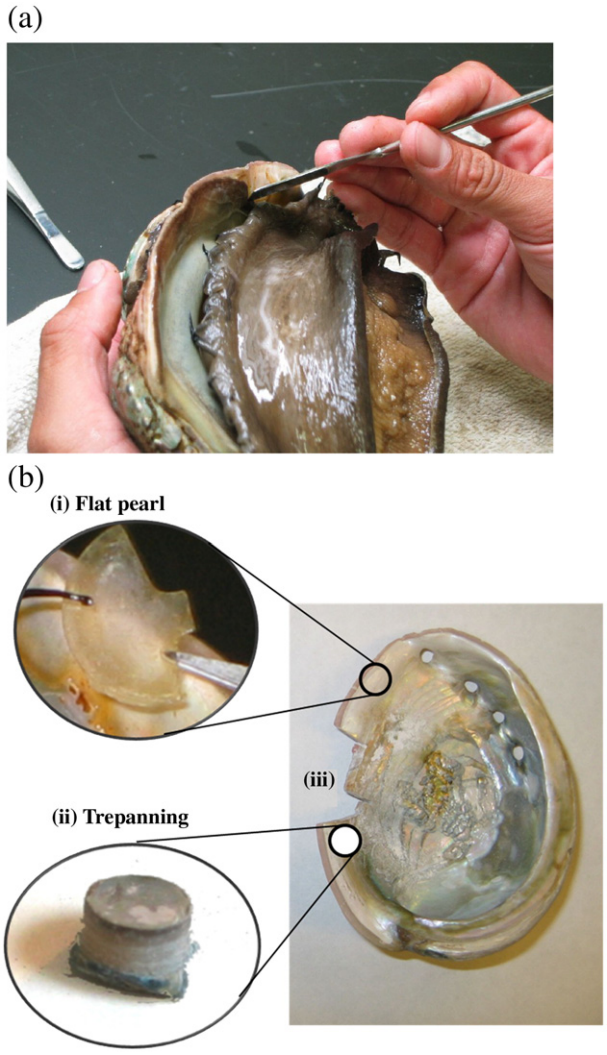

Fig. 2. (a) Abalone shell being manipulated for sample extraction; (b)schematic representation of extraction of specimens for observation and testing of growth surfaces.

elastic modulus of the organic layer. It should be noted that this sagging does not occur in water when growth is taking place.

Coating of the surface and observation in the high vacuum mode produced two significant changes: (a) it improved the resolution significantly, as expected; (b) it produced a shrinking of the organic layer, increasing the incidence of cracks significantly. In some cases these cracks grew during observation. Fig. 4a shows three convergent cracks. These cracks, which were more open than in the environmental mode observation, enabled the excellent observation of terraced growth cones, as shown in Fig. 4(b and c). The three cones in Fig. 4b have approximately 15–18 layers each. This is consistent with their length of 7.5 μm, originating from subsurface tiles and extending through the organic matrix, taking into account that each layer has a thickness of ~0.5 μm. In Fig. 4c one cone is imaged. It was broken off its stem by the force of the shrinking organic layer, as discussed in Section 3.4. Several such incidents were observed. In Fig. 4d the bottom of several cones are seen. An interesting feature is that they all have a central hole. This will be discussed later.

Fig. 5 shows the growth surface in the green (Jeju Island) abalone. In general, the morphology is similar, with the exception that the top tiles are larger as if the top portion of the growth cone had been removed. This presumably happened in the process of extracting the gastropod. The general view, Fig. 5a, shows the folding of organic layer marked by arrows A. It also shows a few tiles that have been bumped off their positions (arrows B). The fact that the tiles can be so easily detached from their neighbors is further evidence that the bonding between neighboring tiles is very weak in the dry condition, as shown by Meyers et al. [27]. Fig. 5(b, c and d) shows details of the top view of individual tiles. It is interesting to note that that none of them have a central hole. The organic layer, which is stretched at the edges of the tiles, shows profuse perforations, as was the case with the observations of Belcher and Gooch [15], and Lin et al. [26]. Another feature that can be seen, albeit barely, is the presence of asperities in the central area of the tile shown in Fig. 5d. The greater occurrence of bridges in the central region as opposed to the periphery was recorded by Song et al. [28,29], Barthelat et al. [13–15], and Tang et al. [30].

This hole in the center of the tile has been a matter of some speculation and it has been proposed by Sarikaya [31] that it houses an organic core that is responsible for providing the genetic message for growth. The idea of a central organic chord transmitting the information for growth up the terraces is attractive. However, the absence of these holes in many specimens (e. g., the green abalone in Fig. 5 and the red abalone grown by the flat pearl method by Lin et al. [24,26] suggests an alternative, simpler mechanism. This is shown in the sequence i–iv of Fig. 6. This alternative view is consistent with the existence of bridges between adjacent layers. As one organic layer is deposed by the inner surface (epithelium) of the mantle, it rests on the top layers of the cones. The growth of the mineral proceeds through the orifices in the organic layer (Fig. 6i), possibly caused by local stretching. Several mineral bridges are simultaneously formed and growth in the new layer radiates from them (Fig. 6ii). The formation of the initial protrusions anchors the organic layer effectively, as shown in Fig. 6iii and v. These growth regions expand laterally as well as away from the interface. A new organic layer is deposited by the mantle every time the thickness is ~0.5 μm (Fig. 6iii and v). A void is trapped in Fig. 6iv, since calcium and carbonate ions can longer reach it. The sequence in Fig. 7 shows a top view of the initiation of growth from three points (bridges that cross the organic layer) and their growth. When the three regions connect a hole is 'trapped' in center (Fig. 7b). It is proposed that the inner layer of the mantle (epithelium) possesses sensors that trigger the deposition of this organic layer periodically (or at every 0.5 μm). At that point, the hole between different growth regions is formed when they touch each other. This region is therefore separated from the external growth regions, which are fed by transport of the Ca^{+2} and CO_3^{-2} ions through the organic layer (Fig. 7c).

3.2. Atomic force microscopy

Atomic force microscopy confirmed all the features observed by scanning electron microscopy and allowed, additionally, detailed observation of the organic layer. Fig. 8a shows the three-dimensional view of the growth surface of the red abalone. The contrast between the higher mineral growth extremities and the underlying organic layer is clear. These mineral protrusions are a few μm high, consistently with the SEM observations. The shapes are somewhat distorted because of the AFM tip, that does not capture very well the lateral details. In a few places lateral ridges due to successive tile layers can be seen and are marked by arrows. The tops of the cones are rounded, consistently with SEM observations. Fig. 8b shows analogous observations for the green abalone. Again, the mineral regions protrude through a flat organic layer. The steps on the lateral surface of the mineral indicate boundaries between tiles and are marked by arrows.

The organic layers of the red and green abalone were also imaged in the dry condition. Fig. 9a shows a region from the red abalone that has significant surface irregularities. However, since the organic layer is in the dried condition, it cannot be ascertained whether this is the real shape. The roughness of the surface could account for the bumps in the surface of the mineral surface. Fig. 9b shows the surface of the

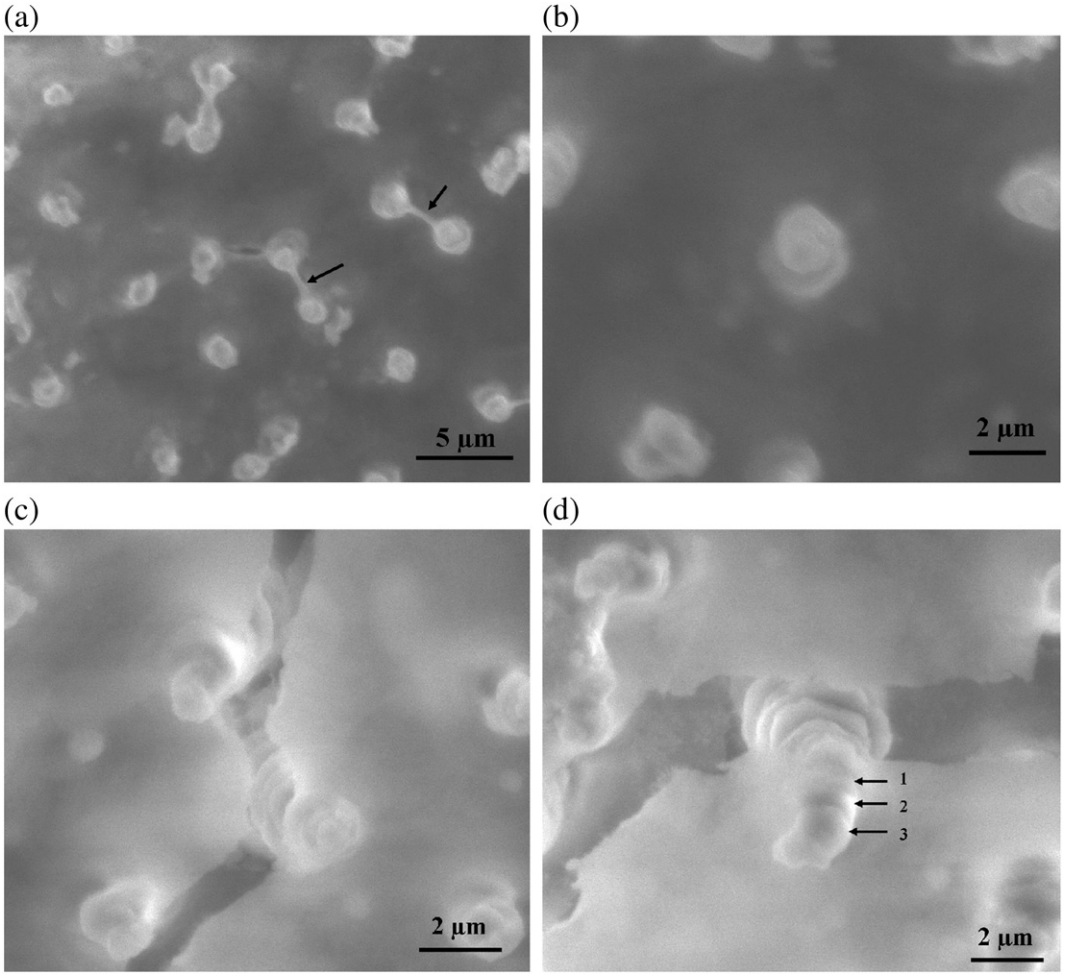

Fig. 3. Growth surface in red abalone (environmental SEM); (a) overall view showing mineral apexes and flat organic layer; (b) detailed view showing top layer of mineral growth; (c, d) cracked organic layer revealing partial details of terraced growth mode. In (a) arrows denote organic 'folds' between adjacent terraced cones. In (b) arrows 1, 2, 3 denote presumed mineral layers under cover of organic layer.

organic layer for the (green) abalone. It has a mottled appearance which could be due to the fact that it is dried. The depth of these irregularities is in the 5 nm range. This is consistent with the bumps observed on the surface of the tiles. The irregularities are of the same order as those in Fig. 6a (red abalone). Thus, one can conclude that, over a distance of 1 μm, they are in the order of 2–10 nm. A possible crack in the organic layer is seen and marked with an arrow in Fig. 9c.

In stark contrast with Fig. 9, the demineralized organic surface imaged in the wet condition reveals a structure of fibrils seen in Fig. 10a. These fibrils have been discussed by Crenshaw and Ristedt [32], Weiner and Traub [33,34], Lowenstein and Weiner [35], Sarikaya [21], Mann [1], and Zentz et al. [36]. There is a consensus that they are the structural component of the intertile organic layer and consist of chitin macromolecules. They are visible in Fig. 10 because the material was demineralized and the acidic macromolecules forming the outside layers were removed, exposing the chitin network. This fibrous network was first identified through AFM by Lin et al. [26]. The chitin fibrils are randomly oriented as shown from the orientation distribution plot in Fig. 10b. Fig. 11 shows the schematic structure of the intertile layer. The chitin fibrils are sandwiched between two layers of acidic molecules. These layers are present in the AFM specimens of Fig. 9 and were dissolved away in Fig. 10. Thus the difference. It should be noted that a more complex structure with two chitin layers has been recently proposed (Pereira-Mouriés [37]); however, it is not discussed here.

The morphologies observed here confirm the growth mechanism based on the formation of bridges that was first proposed by Schäffer et al. [17]. Fig. 12 shows the mechanism operating by the growth of the crystal through holes existing in the organic intertile layer. The epithelial layer that comprises the inside surface of the mantle produces, periodically, the organic intertile layer. This layer slows down the growth of the aragonite in the c direction (which is the direction of rapid growth). It proceeds by the propagation of mineral bridges through holes in the layer. At the same time, lateral growth of the tiles continues because the calcium and carbonate ions can traverse the organic layer through the holes and ion-exchange channels. The cross section is imaged by SEM using the back-scattered mode in the bottom of Fig. 12; the organic intertile layers are darker as a direct consequence of their lower atomic number. Arrows A designate organic interlayers imaged by SEM; arrow B designates a lateral boundary of tile. It is clear that the lateral surfaces of the tiles only possess a much thinner layer of organic material. In the insert, only a faint vertical line indicates the position where two tiles abut. This observation refutes the tridimensional templating mechanism.

Fig. 13a shows a depth profile traced though the line marked in the AFM micrograph of Fig. 13b. This area is also imaged in perspective in Fig. 8b. The depth profile shows steps that correspond to the individual tiles and are marked by the three arrows. The corresponding depth differences are ~500 nm (more exactly, 422

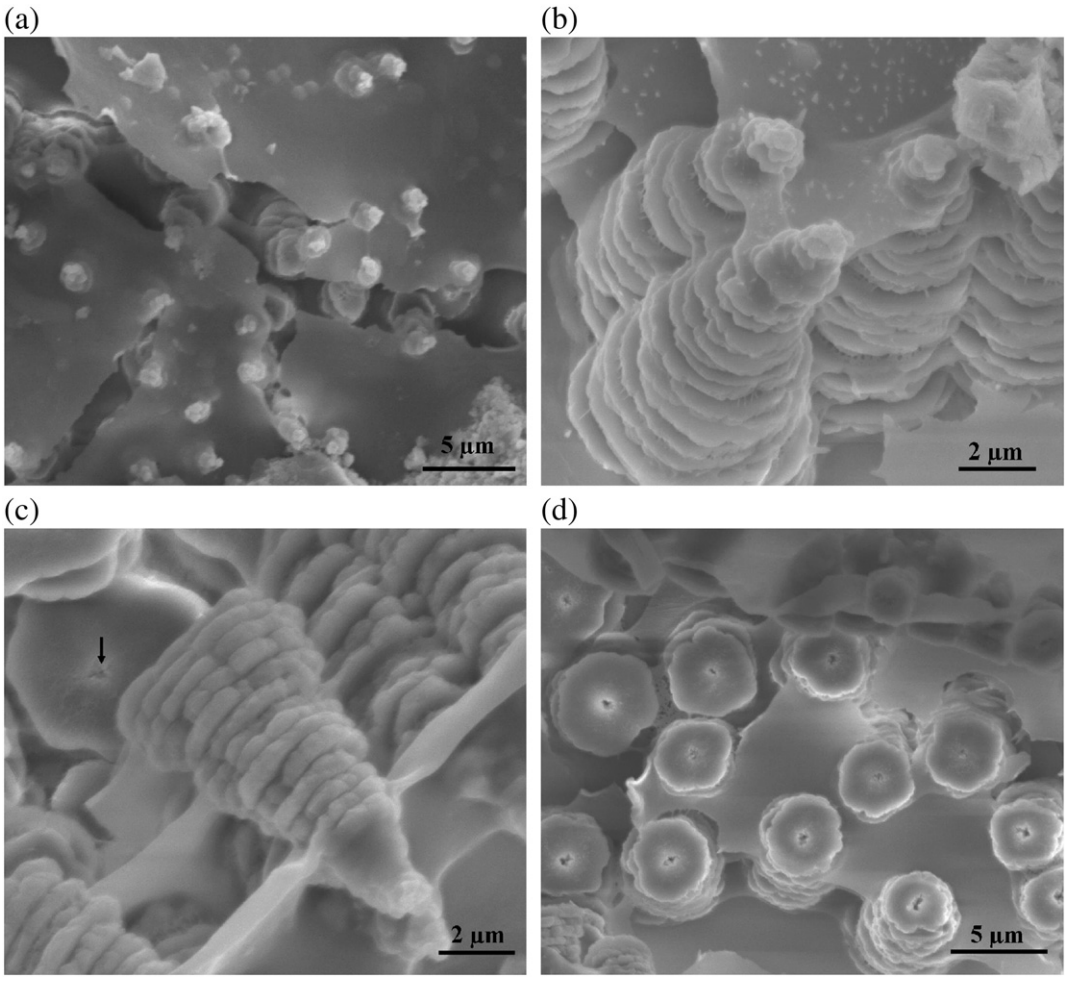

Fig. 4. Growth surface in red abalone (coated specimen, high vacuum SEM); (a) overall view showing mineral apexes and flat organic layer; (b) cracked organic layer; (c) detailed view of three terraced growth sequences; (d) top view of fractured terraced growth sequences exposing incompletely grown tiles with central holes. Arrow in (c) denotes central core orifice revealed by fracture of terraced cone.

and 456 nm). This corresponds to the tile thickness. The different tile layers can also be seen in the AFM micrograph of Fig. 8b. The tops of the tiles are flat, in agreement with the SEM of Fig. 5. This proved to be quite useful for nanoindentation testing, reported in Section 3.3.

The drastic difference in mechanical response between wet and dry organic intertile layer is attributed to two factors:

a) The chitin network is at a temperature below its glass transition temperature, which is around 200 °C for chitosan (Sakurai et al. [38]). This is a macromolecule that is a deacetilated form of chitin which has a storage modulus E' ~10 GPa and a loss modulus E'' ~0.1 GPa at ambient temperature.
b) The organic intertile layer acts essentially like a hydrogel. The strength of chitosan-based hydrogels has been established (Lee et al. [39]) and varies from 0.06 MPa, in the fully hydrated condition, whereas that of the dry compound is ~5 MPa. This is close to a hundred-fold increase.

Hence, the mantle of the abalone deposits the organic intertile layer when the growth of the tops of the terraced cones has reached 0.5 μm. This layer is anchored by the growth of minerals through pores. The growth of the aragonite crystals is retarded in the c direction, creating the tiled configuration.

3.3. Nanoindentation testing

The primary objective of nanoindentation testing was to obtain some information on the mechanical response of the organic layer. The Berkovich indenter was used on three areas in the dry condition: fully grown shell; top of growth cones; organic region. The fully grown region is located behind the growth front in the shell and corresponds to the layer that can be visually identified by the mother-of-pearl appearance. The results of several indentation tests are shown in Fig. 14a. The average hardness and Young's modulus, from five tests, are ~2.7 and 34 GPa, respectively. The results are consistent with the ones obtained by Barthelat et al. [41–43] on red abalone. They performed nanoindentation tests at different loads (and indentation depths) and observed an effect of load. For a depth of ~100 nm, they report a best fit result for the hardness and Young's modulus of 1.1 GPa and 33 GPa, respectively. These results are considerably lower than the ones reported by Bruet and coworkers [40] for the gastropod mollusc *Trochus niloticus*: 9 and 79 GPa, respectively, for samples soaked in salt water. However, the latter results are from FEM analysis while the Barthelat et al. [41–43] results are from direct conversion of the measurements using the standard Oliver-Pharr equation. By eliminating the effect of the organic layer through FEM, Barthelat et al. [41–43] arrived at E = 80 GPa, in agreement with Bruet et al. [40]. The dry samples exhibited values that were even higher: 11 and 92 GPa.

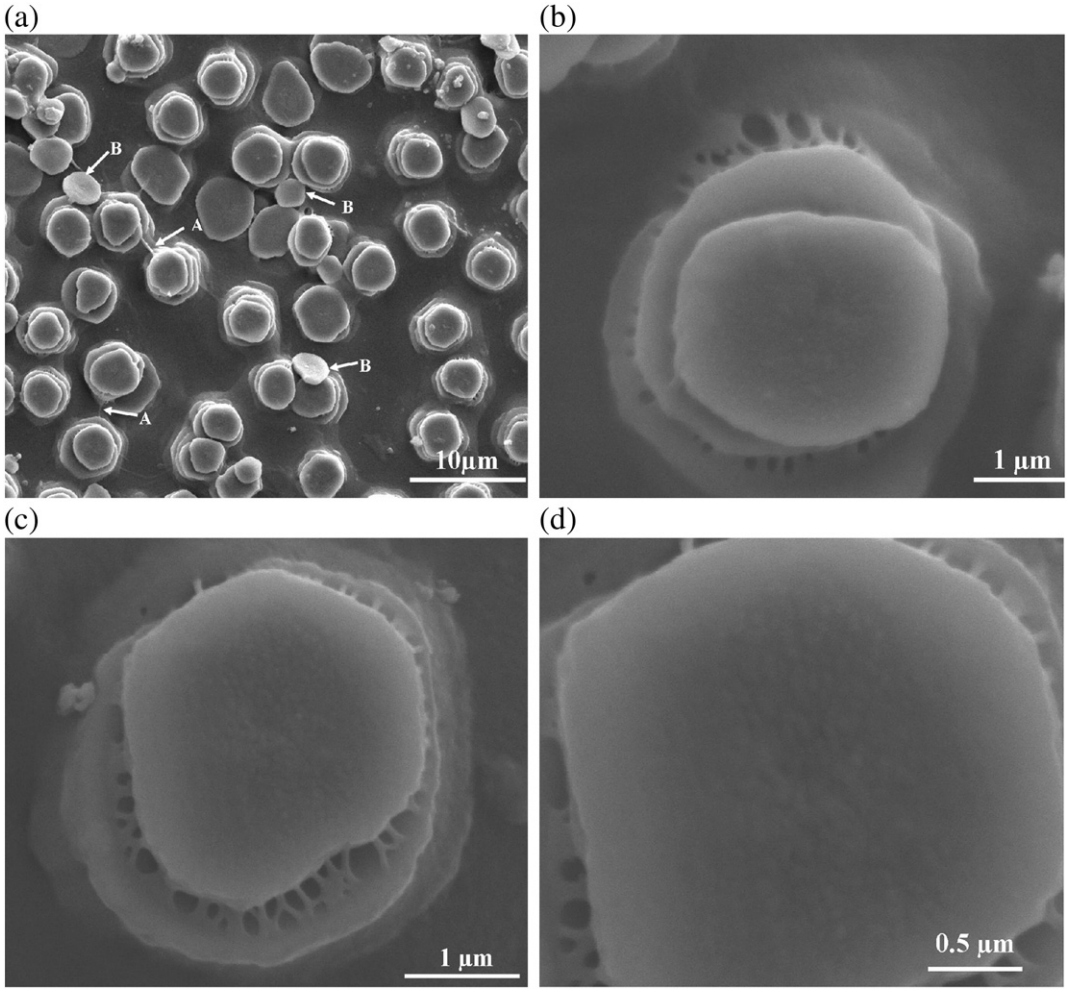

Fig. 5. Growth surface in green abalone (environmental SEM); (a) overall view showing mineral apexes and flat organic layer; (b, c) stretched organic layer around tile exposing pattern of holes; (d) top view of individual tile with surface irregularities. In (a) arrows A denote organic 'folding' between adjacent mineral stacks; arrows B denote mineral tiles that were knocked off their original positions.

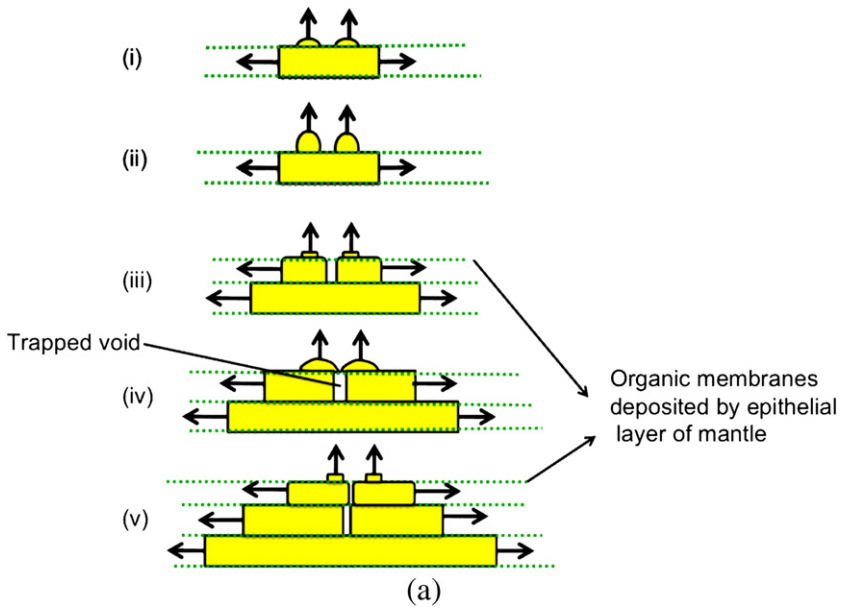

Fig. 6. Growth of mineral through the organic interlayer that is periodically deposited by the epithelial layer of the mantle (as described by Mann [1], p. 78); multiple penetration of mineral bridges through organic layer and connection, trapping the void.

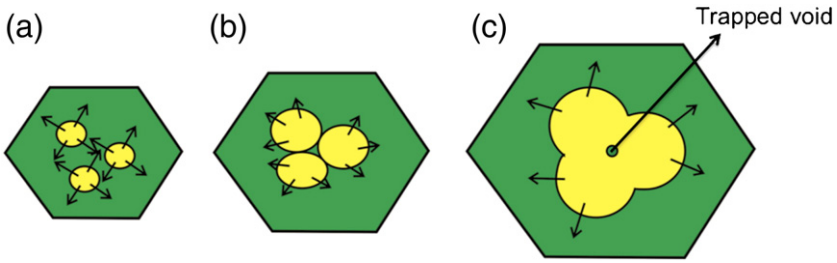

Fig. 7. Proposed sequence of formation of central hole in red abalone through trapping of growth by sequential growth; (a) mineral bridges that just traversed holes in the organic layer; (b) lateral growth of mineral bridges; (c) outward expansion of tile growth leaving internal void trapped.

However, this shell has thicker tiles (~0.9 μm). The green (Jeju) abalone in which the tests were made was out of water for, at most, 7 days. The accuracy of the measurement was established by using a fused quartz standard with the same support consisting of Tack-it. The value, 61.2 GPa, was 10% below the standard elastic modulus, which is 69.6 GPa. However, it cannot account for the large difference between the current results and those of Bruet et al. [40].

Indentations on the tops of the terraced cones for the Jeju (green) abalone were made, since they provided flat platforms of sufficient size, as shown in Fig. 5. The average indentation diameter was 2 μm, and there was sufficient space for the measurement. On the other hand, such measurements could not be made on the top of the terraces in the red abalone. Typical nanoindentation curves are shown in Fig. 14b. The average hardness and elastic moduli from three tests are, respectively, 2.12 and 23.2 GPa. This is somewhat lower but consistent with the results on the shiny, mother-of-pearl portion of the shells. One of the curves shows a shift to the right at constant load that is attributed to the fracture of the tile.

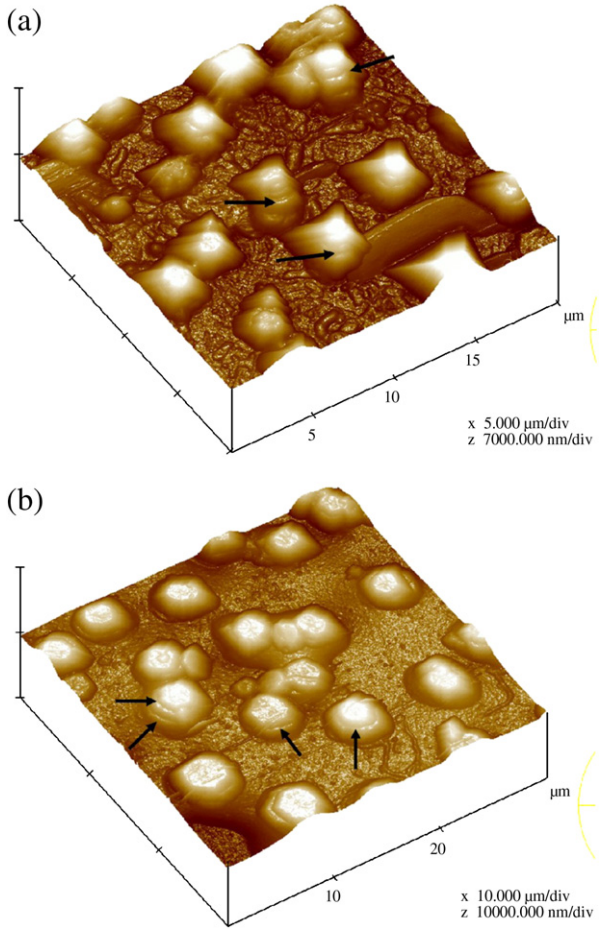

Fig. 8. Atomic force microscopy of (a) red and (b) green abalone in tridimensional representation; arrows denote boundary between successive layers in stacks (terraced cones).

The measurement of the mechanical properties of the organic layer is much more challenging. Meyers et al. [27] used the sag of the organic layer to estimate the elastic modulus and obtained a value of 100 Pa. In the current investigation, the Berkovich indenter was centered on the regions between mineral cones. The descending indenter encountered an organic membrane and deflected it downward until it deformed inelastically, ruptured, met a lower membrane, or encountered the underlying mineral. Examples of these three events were observed. Experiments were carried out for both the green and red abalone, and typical curves are shown in Fig. 15. The change in slope in the indentation curves for both red and green abalone specimens in Fig. 15 indicates two regimes, the first corresponding to membrane deformation, and the second contact with the mineral. For the red abalone specimen, the change of response occurred for three tests at ~500 nm. For the green abalone, Fig. 15b, the change of slope occurs at a deflection of approximately 300–400 nm. One should also consider that there is some 'sag' in the membranes which decreases the distance. These values correspond approximately to one tile layer. If one recalculates the load-deflection curve subtracting this quantity, one obtains a hardness value closer to the mechanical response of the mineral: 0.5 GPa.

Fig. 16a shows a schematic configuration of an indenter deforming the organic intertile layer. The membrane is supported by three mineral columns. Fig. 16b and c show the situations where the organic layer is deflected. In Fig. 16b the indenter encounters the mineral at a depth of 400–500 nm, whereas in Fig. 16c the gap is such that the indenter continues to descend, touching the underlying organic layer. It is felt that for the green abalone the situation of Fig. 16b is prevalent, whereas for the red abalone the configuration is such that the indenter can encounter the mineral after two or three layers of organic (1000 or 1500 nm, respectively), shown in Fig. 16a.

The schematic in Fig. 17 assumes that the organic layer deflects as a membrane. It is possible to relate the indentation force to the deflection through the elastic modulus of the membrane. A two-dimensional analysis is given below, following the schematic of Fig. 17a. It is possible to obtain a relationship between the force F and deflection δ assuming that the membrane is replaced by a strip with a width equal to the separation between mineral cones and having an elastic modulus E. We have, in Fig. 17b:

$$F = 2F_1 \cos\theta \tag{1}$$

The deflection is:

$$BD = \delta = AB\cos\theta \tag{2}$$

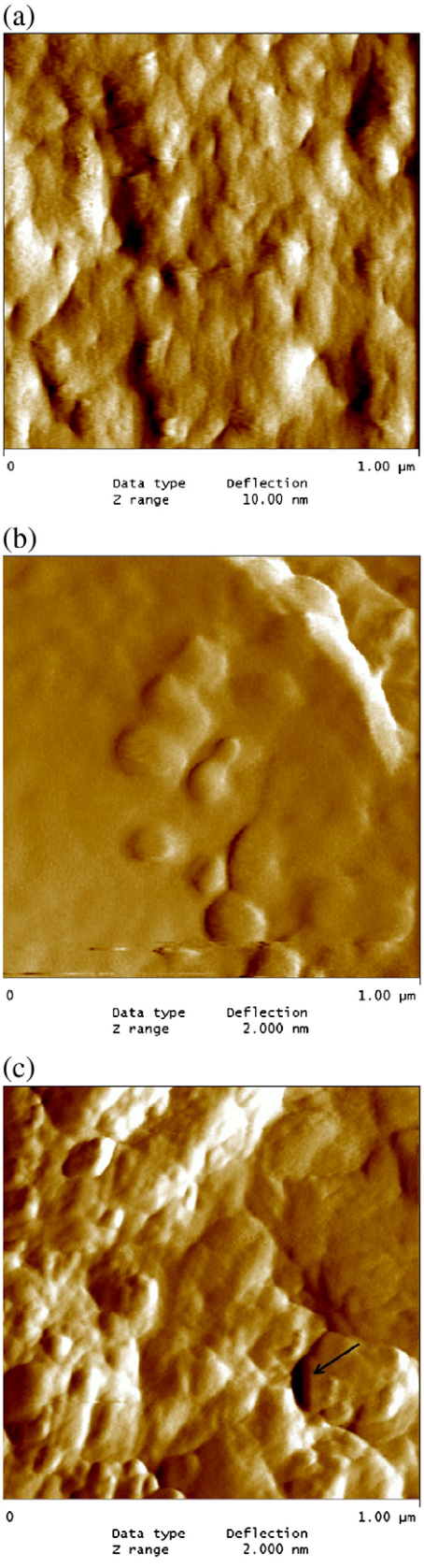

Fig. 9. Surface irregularities in organic layer of red and green abalone; (a) red abalone, max. deflection 10 nm; (b) green abalone, max. deflection 2 nm; (c) crack formed at fold, max. deflection 2 nm.

The strain in segments AB and BC can be expressed as:

$$\varepsilon = \frac{AB - L/2}{L/2} \tag{3}$$

where L is the initial length of the beam and AB its instantaneous half-length. The force F_1 can be equated to the strain through the modulus of the spring, E, and its cross-sectional area, A:

$$F_1 = EA\varepsilon. \tag{4}$$

By using Eq. (3) one obtains:

$$F_1 = EA\frac{AB - L/2}{L/2} \tag{5}$$

But:

$$\cos\theta = \frac{\delta}{AB}. \tag{6}$$

Substitution of Eqs. (5) and (6) into Eq. (1) yields:

$$F = 2EA\frac{AB - L/2}{L/2}\cos\theta = 2EA\delta\left(\frac{1}{L/2} - \frac{1}{AB}\right) \tag{7}$$

But:

$$AB = \sqrt{\delta^2 + L^2/4}.$$

Thus:

$$F = 2EA\delta\left(\frac{1}{L/2} - \frac{1}{\sqrt{\delta^2 + L^2/4}}\right). \tag{8}$$

One can estimate the elastic modulus of the membrane assuming that its cross-sectional area is Lt, where t is the membrane thickness. This assumes that a width of L contributes to the deflection. Fig. 17b shows a plot of force vs. deflection. The following characteristic values were used:

$L = 5\mu m$
$t = 30nm$
$A = Lt$.

The elastic modulus that had to be assumed to obtain values reasonably close to those in Fig. 15 is exceedingly high: 100 GPa. This value is typical of minerals and much higher than the one for chitin that is on the order of 1–3 GPa, if one considers that it is the same as chitosan. Neither the shape of the curve nor the magnitude of the elastic modulus are consistent with an elastic membrane deflection.

Thus, one cannot attribute the response to elastic deformation of the membrane. Indeed, the indentation curves in Fig. 15 show significant non-elastic (permanent) deformation upon unloading. The only alternative mechanism that can be envisaged is deformation of the organic either generalized as in Fig. 16c or localized under the indenter, as shown in Fig. 18. The deformation of the organic layer is localized under the indenter.

The current results suggest that the organic layer becomes very stiff once it dries. This is consistent with the fact that it has a T_g of ~200 °C. The response observed here is in stark contrast with the earlier estimate by Meyers et al. [27] and with the large maximum

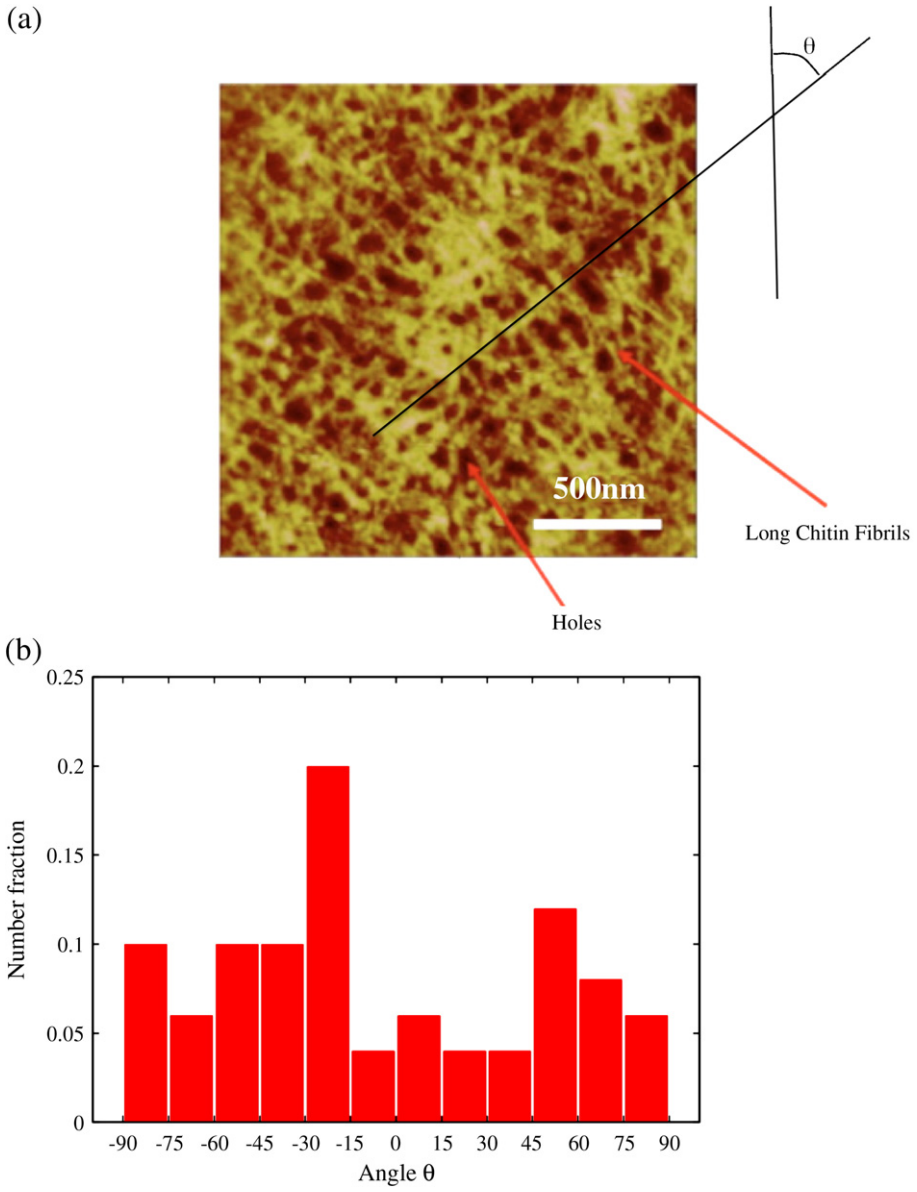

Fig. 10. (a) Chitin fibrils exposed in organic intertile layer obtained by demineralizing nacre (wet AFM); (b) distribution of angle θ of fibrils.

extension measured by Belcher and Gooch [15]. One must conclude that as the organic layer dries, its mechanical response changes drastically. Lee et al. [39] created a polymer network with chitosan and demonstrated that it is a hydrogel, with an equilibrium water content of 74–94%. The tensile strength of a mixture with 75% chitosan in the swollen state was ~60 kPa, whereas in the dry state it is around 5 MPa. This is a decrease of close to hundred fold. Indeed, this had a significant effect on our understanding of the mechanical response of the abalone. Cross polymerization must take place and in this respect the organic layer can play a significant role in the tensile strength of the shell when the force is applied parallel to the shell surface. The fact that the organic layer cracks when dried and/or when it is observed by SEM is further evidence that it hardens significantly.

3.4. Breaking of terraced cones

The observation of broken-off terraced cones can be explained by the schematic plot of Fig. 19 that shows the force F exerted by the shrinking organic layer. It is possible to estimate the resistance to fracture of the cone, since the tensile strength of the mineral bridges as well as their number has been estimated by Meyers et al. [27] based on measurements by Song et al. (2002, 2003). Fig. 19b shows the resistance to the flexure moment $M_m = F_m h$ applied to the cone by the organic layer. The maximum stress that each bridge can withstand is (see Meyers et al. [27] and Gao and coworkers [44–46]:

$$\sigma_{th} = \frac{E}{30}. \tag{9}$$

The resisting moment from the bridges is:

$$M_r = \sum_{i=1}^{n} F_i X_i \tag{10}$$

where F_i is the force exerted by the i'th bridge, which is at a distance X_i from pivoting point O (Fig. 19b). There are n bridges per tile,

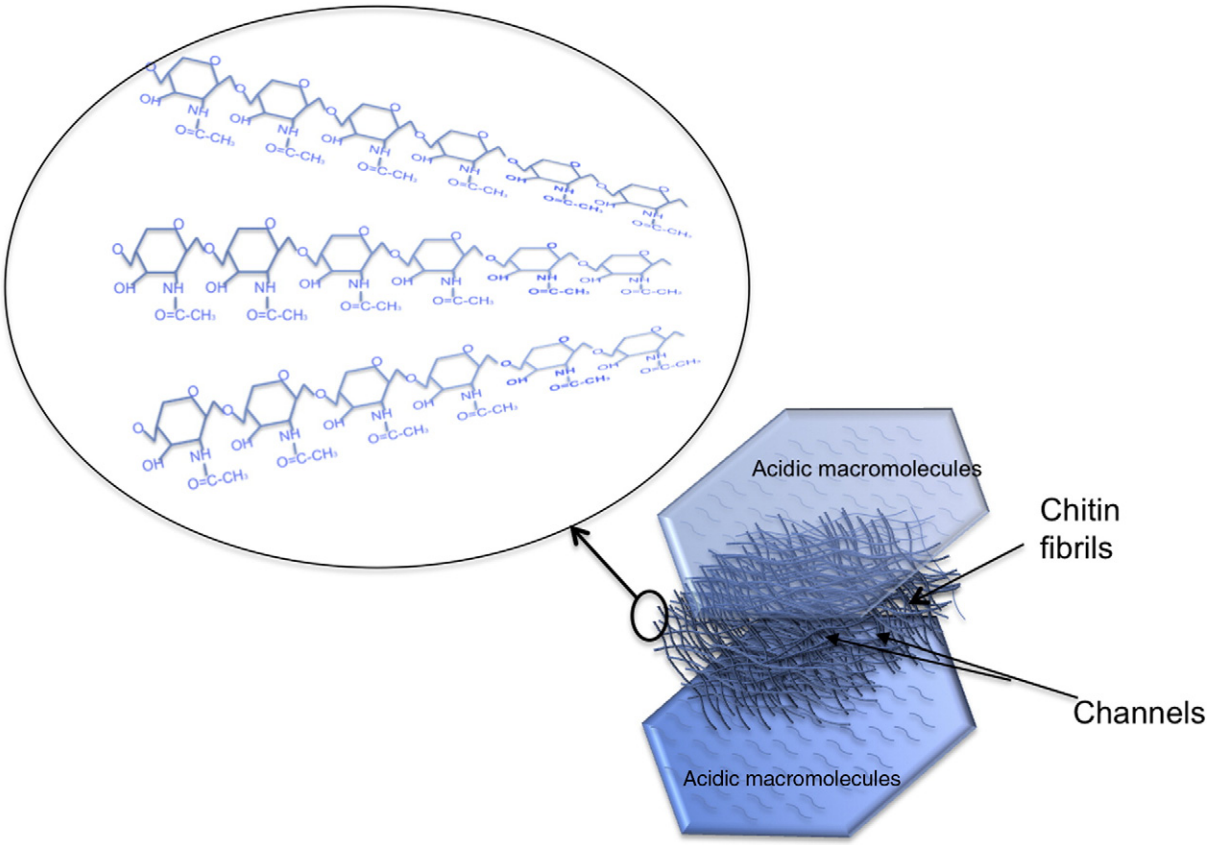

Fig. 11. Schematic representation of organic intertile layer consisting of central layer with randomly oriented chitin fibrils sandwiched between.

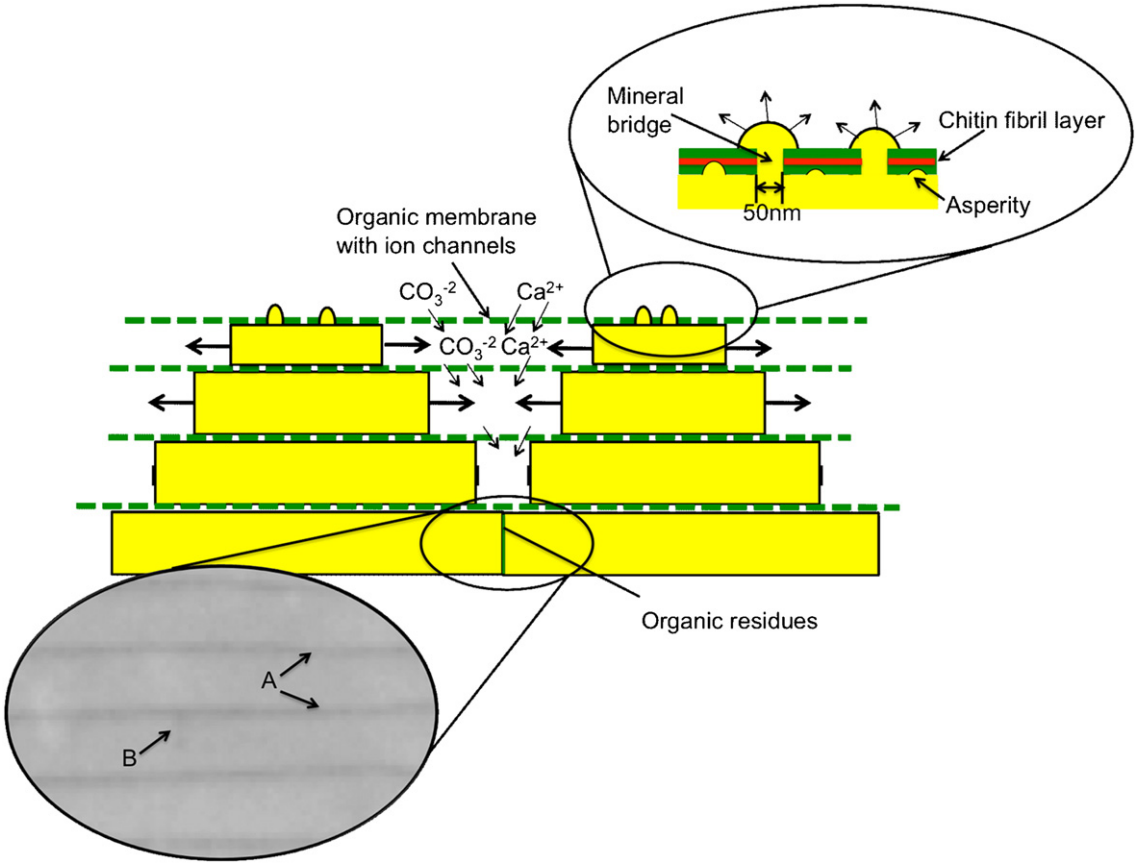

Fig. 12. Mechanism of growth of nacreous tiles by formation of mineral bridges; organic layer is permeable to calcium and carbonate ions which nourish lateral growth as periodic secretion and deposition of the organic intertile membranes restricts their flux to the lateral groth surfaces. Arrows A designate organic interlayer imaged by SEM; arrow B designates lateral boundary of tile.

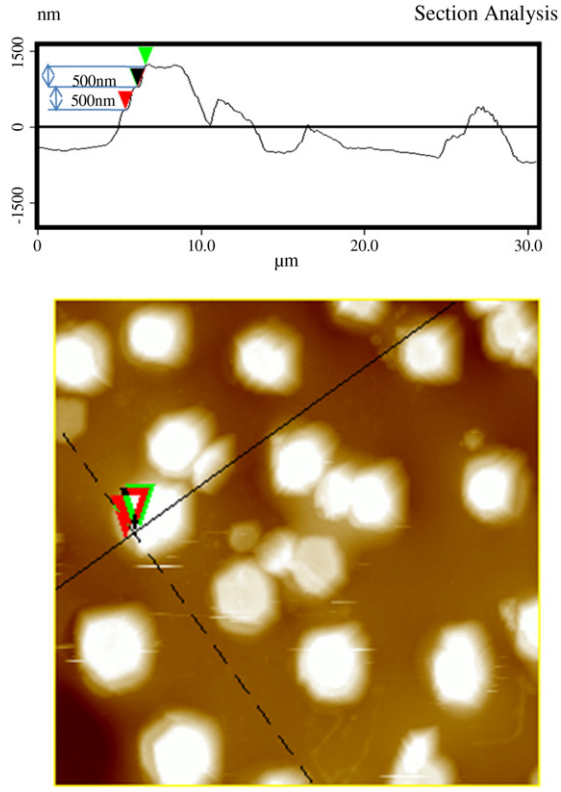

Fig. 13. Atomic force microscopy of green abalone: mineral tiles protruding from surface profile along line indicated in micrograph (vertical distances, between lines ~500 nm).

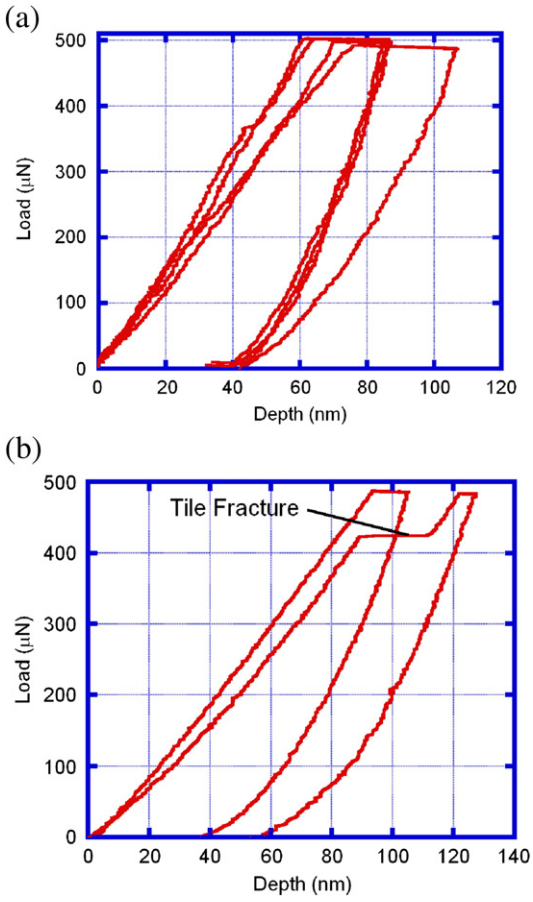

Fig. 14. Nanoindentation hardness of (a) completely mineralized region (red abalone); (b) tops of terraced cones (green abalone).

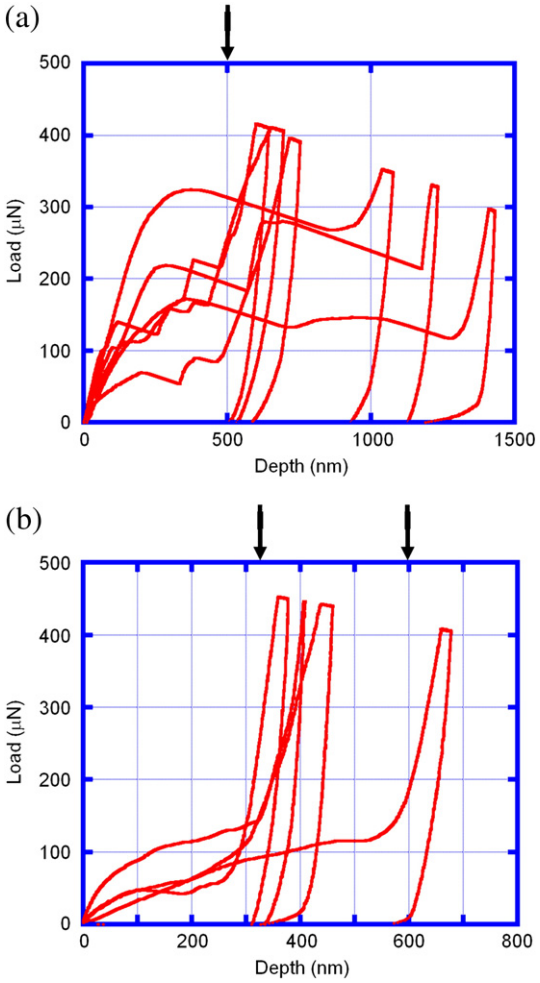

Fig. 15. Nanoindentation hardness for organic layer; (a) red abalone; (b) green abalone.

concentrated in the central region. We assume that they are uniformly distributed in a central region with radius R_0 such that:

$$D/2 + R_0 \geq X_i \geq D/2 - R_0. \quad (11)$$

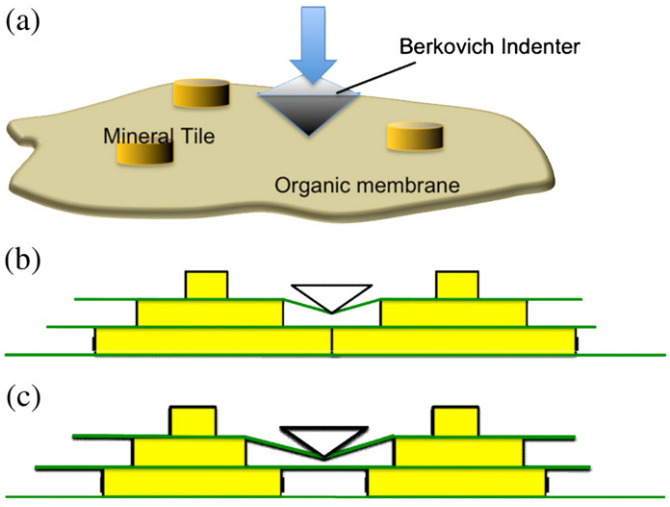

Fig. 16. Representation of nanoindenter deforming organic layer; (a) tridimensional representation of indenter deforming organic layer; (b) configuration of single organic layer with a mineral underneath; (c) configuration of organic layer that is joined with lower level by deflection.

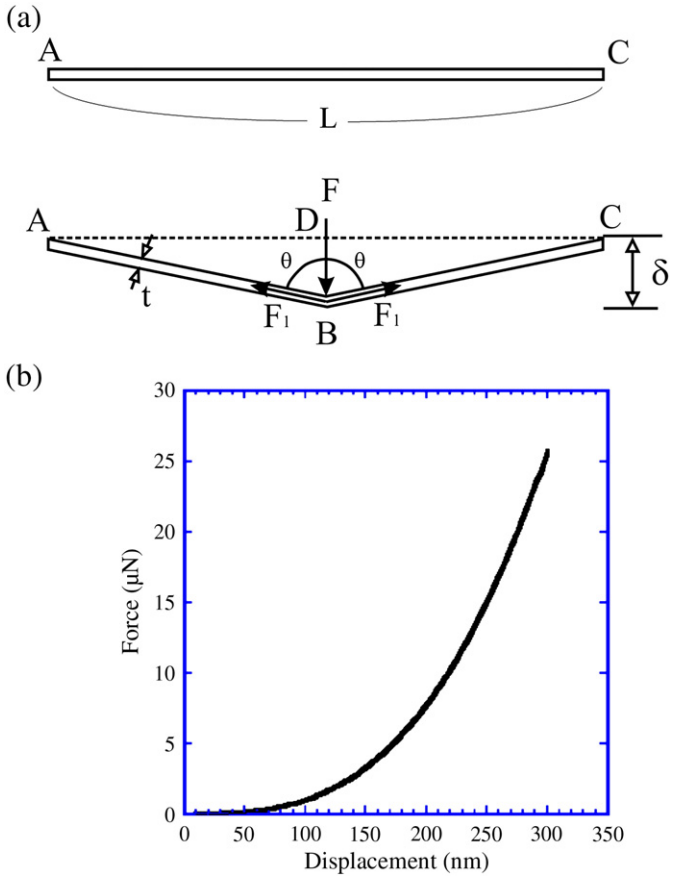

Fig. 17. (a) Two-dimensional representation of membrane being deflected elastically by local force at center. (b) Force-displacement plot using elastic deflection equation assuming $E = 100$ GPa.

The resisting force varies linearly with distance from the pivot point O. Thus:

$$\frac{F_{\max}}{D/2 + R_0} = \frac{F_i}{X_i}. \tag{12}$$

We assume that all the bridges have the same radius r. The maximum force can be expressed as a function of the theoretical stress, given in Eq. (13):

$$F_{\max} = \pi r^2 \sigma_{th} = \frac{\pi r^2 E}{30}. \tag{13}$$

The expression for the total resisting moment becomes:

$$M_r = \sum_{i=1}^{n} \frac{F_{\max}}{D/2 + R_0} X_i^2 = \frac{\pi r^2 E}{30(D/2 + R_0)} \sum_{i=1}^{n} X_i^2. \tag{14}$$

We have to assume a distribution of bridge sites. The simplest approach is to assume a square grid with dimensions $2R_0$. This is shown in Fig. 19b. There are $I(\sqrt{n})$ rows (where I is the closest integer to $\sqrt{n}$) with distances X_i equal to:

$$X_i = D/2 - R_0; (D/2 - R_0) + 2\frac{R_0}{\sqrt{n}}; (D/2 - R_0) + 4\frac{R_0}{\sqrt{n}}; \ldots..; (D/2 - R_0) + 2\sqrt{n}\frac{R_0}{\sqrt{n}} \tag{15}$$

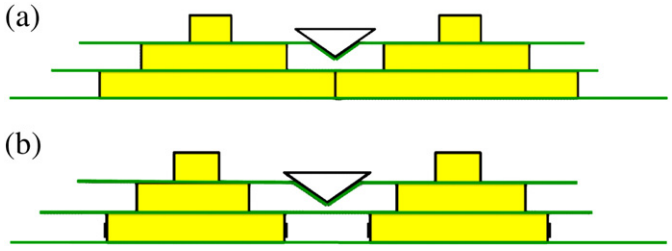

Fig. 18. Localized permanent deformation mode of organic membrane; (a) indenter reaches mineral after one tile layer; (b) indenter reaches second layer prior to reaching mineral.

The outer bridges in the column will fail when:

$$M_r = M_m = F_m h. \tag{16}$$

It is possible to calculate this value from parameters characteristic of the abalone nacre. We assume:

n	$= 36$ (estimate from Song et al. [28,29] and Meyers et al. [27])
h	$= 10$ μm (from Fig. 3c)
D	$= 10$ μm
$2r$	$= 50$ nm
$2R_0$	$= D/2$ (estimate based on observations of Song et al. [28,29])
E	$= 100$ GPa.

This yields $M_m \approx 0.84 \times 10^{-9}$ N•m. The corresponding force ($h = 10$ μm) is:

$$F_m \approx 84\ \mu N. \tag{17}$$

As seen in Section 3.3, this force is on the order of the force required for the nanoindenter to rupture the organic membrane. In Fig. 15, one can consider, to a first approximation, the force that the organic layer can resist varies from 50 to 200 μN. Thus, one can conclude that the shrinking organic layer can exert a force of sufficient magnitude to produce flexure fracture in the terraced growth columns.

4. Conclusions

The AFM characterization combined with nanoindentation testing provided a novel means of probing of the organic interlayer and enabled the following conclusions to be drawn:

1. The growth proceeds by the terraced cone mechanism. The mineral component grows through bridges that traverse the organic intertile layer and ensure the same crystallographic orientation in tiles that are part of the same terraced cone (or stack). Additional evidence that the bonding between adjacent tile layers is weak in the dry state and confined to the bridges was uncovered.
2. It was possible to deform the organic layer with the Berkovich nanoindenter; rather than deflect elastically in a membrane mode, the organic layer underwent permanent deformation (and/or fracture) which may distributed over the membrane or confined to the region under the indenter. This indicates that the membrane strength and stiffness are significant.
3. The breaking of growth terraces by the shrinking organic layer is consistent with the strength of the mineral bridges estimated earlier by Meyers et al. [27] and bridge density measured by Song et al. [28,29].
4. The current results in combination with earlier observations (Lin et al. [26]; Meyers et al. [27]) suggest that the organic intertile layer is initially very soft and pliable and gradually hardens as it dries.

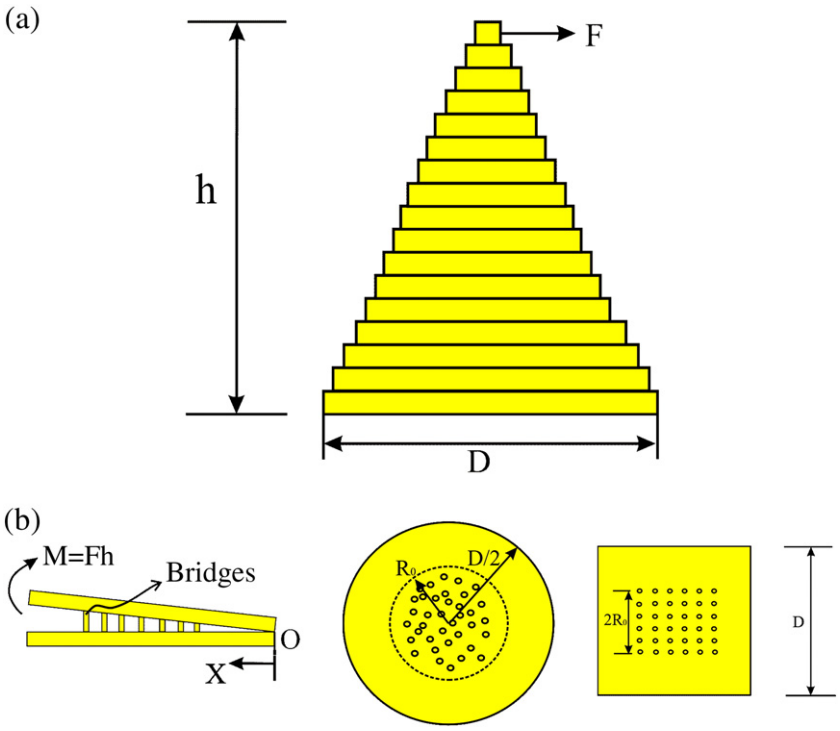

Fig. 19. (a) Schematic representation of terraced cone subjected to force *F* exerted by organic layer; (b) bridges subjected to tension; (d) schematic arrangement of bridges; (d) idealized arrangement in 6×6 matrix.

This factor is significant and explains how the mantle can mold the initially soft material that subsequently hardens into a high-toughness ceramic-organic composite. The major structural component of the interlayer, chitin, has a glass transition temperature of approximately 200 °C. It also has great ability to absorb water, forming a hydrogel that stiffens upon being dehydrated.

Acknowledgement

This research is supported by the National Science Foundation Grant DMR 0510138. Discussions with Dr. A. Y. M. Lin and Mr. P.-Y. Chen are gratefully acknowledged. Julie Muyco provided the AFM picture of Fig. 11a.

References

[1] S. Mann, Biomineralization: Principles and Concepts in Bioinorganic Materials Chemistry, Oxford U. Press, 2001.
[2] I. Kobayashi, T. Samata, Mater. Sci. Eng. C 26 (2006) 692.
[3] G. Bevelander, H. Nakahara, Calc. Tissue 3 (1969) 84.
[4] G. Bevelander, H. Nakahara, in: M. Omori, N. Watabe (Eds.), The Mechanisms of Biomineralization in Animals and Plants, Tokai University Press, Tokyo, 1980, p. 19.
[5] K. Wada, Biomineralization 6 (1972) 84.
[6] H. Nakahara, Venus 38 (1979) 205.
[7] G. Bevelander, H. Nakahara, M. Kakei, Venus Jpn. J. Malac. 41 (1982) 33.
[8] H. Nakahara, in: P. Westbroek, E.W. De Jong (Eds.), Biomineralization and Biological Metal Accumulation, D. Reidel Publishing Company, Dordrecht, Holland, 1982, p. 225.
[9] H. Nakahara, in: S. Suga, H. Nakahara (Eds.), Mechanisms and Phylogeny of Mineralization in Biological Systems, Springer-Verlag, New York, 1991, p. 343.
[10] H. Mutvei, in: M. Omori, N. Watabe (Eds.), The Mechanisms of Biomineralization in Animals and Plants, Tokai Univ. Press, 1980.
[11] M. Fritz, A.M. Belcher, M. Radmacher, D.A. Walters, P.K. Hansma, G.D. Strucky, D.E. Morse, Nature 371 (1994) 49.
[12] M. Fritz, D.E. Morse, Col. Int. Sci. 3 (1998) 55.
[13] A.M. Belcher, X.H. Wu, R.J. Christensen, P.K. Hansma, G.D. Stucky, D.E. Morse, Nature 381 (1996) 56.
[14] A.M. Belcher, PhD thesis: Spatial and temporal resolution of interfaces, phase transitions and isolation of three families of proteins in calcium carbonate based biocomposite materials, University of California, Santa Barbara 1997.
[15] A.M. Belcher, E.E. Gooch, in: E. Bauerlein (Ed.), Biomineralization: from biology to biotechnology and medical application, Wiley-Interscience, Germany, 2000, p. 221.
[16] X.Y. Shen, A.M. Belcher, P.K. Hansma, G.D.S. Stucky, D.E. Morse, J. Biol. Chem. 272 (1997) 32472.
[17] T.E. Schäffer, C. Ionescu-Zanetti, R. Proksch, M. Fritz, D.A. Walters, N. Almqvist, C.M. Zaremba, A.M. Belcher, B.L. Smith, B.L. Smith, G.D. Stucky, D.E. Morse, P.K. Hansma, Chem. Mater. 9 (1997) 1731.
[18] C.M. Zaremba, A.M. Belcher, M. Fritz, Y. Li, S. Mann, P.K. Hansma, D.E. Morse, J.S. Speck, G.D. Stucky, Chem. Mater. 8 (1996) 679.
[19] M. Sarikaya, K.E. Gunnison, M. Yasrebi, J.A. Aksay, Mater. Res. Soc. 174 (1990) 109.
[20] M. Sarikaya, J.A. Aksay, in: S. Case (Ed.), Results and Problems in 'Cell Differentiation in Biopolymers', Springer, Amsterdam, 1992, p. 1.
[21] M. Sarikaya, Microsc. Res. Tech. 27 (1994) 360.
[22] M. Sarikaya, J. Microsc. Res. Technol. 427 (1994) 360.
[23] J.H.E. Cartwright, A.G. Checa, J. R. Soc. Interface 4 (2007) 491.
[24] A. Lin, M.A. Meyers, Mater. Sci. Eng. A 390 (2005) 27.
[25] A.Y.M. Lin, M.A. Meyers, K.S. Vecchio, Mater. Sci. Eng. C 26 (2006) 1380.
[26] A.Y.M. Lin, P.Y. Chen, M.A. Meyers, Acta Biomater. 4 (2008) 131–138.
[27] M.A. Meyers, A.Y.M. Lin, P.Y. Chen, J. Muyco, J. Mech. Behav. Biol. Mater. 1 (2008) 76.
[28] F. Song, X.H. Zhang, Y.L. Bai, J. Mater. Res. 17 (2002) 1567.
[29] F. Song, A.K. Soh, Y.L. Bai, Biomaterials 24 (2003) 3623.
[30] H. Tang, F. Barthelat, H.D. Espinosa, J. Mech. Phys. Solids 55 (2007) 1410.
[31] M. Sarikaya, private communication, 2001.
[32] M.A. Crenshaw, H. Ristedt, in: N. Omori, N. Watabe (Eds.), The mechanisms of Biomineralization in Animals and Plants, Tokay U. Press, 1976.
[33] S. Weiner, W. Traub, FEBS Lett. 111 (1980) 311.
[34] S. Weiner, W. Traub, Philos. Trans. R. Soc. B 304 (1984) 421.
[35] H.A. Lowenstam, S. Weiner, On Biomineralization, Oxford U Press, 1989.
[36] F. Zentz, L. Bedouet, M.J. Almeida, C. Milet, E. Lopez, M. Giraud, Mar. Biotechnol. 3 (2001) 36.
[37] L. Pereira-Mouriés, M.-J. Almeida, C. Ribweiro, J. Peduzzi, M. Barthélemy, C. Milet, E. Lopez, Eur. J. Biochem. 269 (2002) 4994.
[38] K. Sakurai, T. Maegawa, T. Takahashi, Polymer 41 (2000) 7051–7056.
[39] S.J. Lee, S.S. Kim, Y.M. Lee, Carbohydr. Polym. 41 (2000) 197.
[40] B.J.F. Bruet, H.J. Qi, M.C. Boyce, R. Panas, K. Tai, L. Frick, C. Ortiz, J. Mater. Res. 20 (2005) 2400.
[41] F. Barthelat, C.M. Li, C. Comi, H.D. Espinosa, J. Mater. Res. 21 (2006) 1977.
[42] F. Barthelat, H.D. Espinosa, Exp. Mech. 47 (2007) 311–324.
[43] F. Barthelat, H. Tang, P.D. Zavattieri, C.-M. Li, H.D. Espinosa, J. Mech. Phys. Solids 55 (2007) 306.
[44] H.J. Gao, B.H. Ji, I.L. Jäger, E. Arzt, P. Fratzl, Proc. Natl. Acad. Sci. U. S. A. 100 (2003) 5597.
[45] B.H. Ji, H.J. Gao, K.J. Hsia, Philos. Mag. Lett. 84 (2004) 631.
[46] B.H. Ji, H.J. Gao, J. Mech. Phys. Solids 52 (2004) 1963.